Ex-situ tracking solid oxide cell electrode microstructural evolution in a redox cycle by high resolution ptychographic nanotomography

De Angelis, Salvatore; Jørgensen, Peter Stanley; Esposito, Vincenzo; Hsiao Rho Tsai, Esther ; Holler, Mirko; Kreka, Kosova; Abdellahi, Ebtisam; Bowen, Jacob R.

Published in:
Journal of Power Sources

Link to article, DOI:
10.1016/j.jpowsour.2017.06.035

Publication date:
2017

Document Version
Peer reviewed version

Title: Ex-situ tracking solid oxide cell electrode microstructural evolution in a redox cycle by high resolution ptychography nanotomography

Salvatore De Angelis[a], *Peter Stanley Jørgensen*[a], *Vincenzo Esposito*[a], *Esther Hsiao Rho Tsai*[b] , *Mirko Holler*[b], *Kosova Kreka*[a], *Ebtisam Abdellahi*[a], *and Jacob R. Bowen*[a]

a) Department of Energy Conversion and Storage, Technical University of Denmark (DTU), Frederiksborgvej 4000, Denmark

S.D. Angelis: sdea@dtu.dk, P.S.Jørgensen: psjq@dtu.dk, V. Esposito: vies@dtu.dk, K. Kreka: kkre@dtu.dk, E. Abdellahi: ebab@dtu.dk, J. R. Bowen: jrbo@dtu.dk

b) Paul Scherrer Institute (PSI),

5232 Villigen, Switzerland

E. H. R. Tsai: esther.tsai@psi.ch, M. Holler: mirko.holler@psi.ch

Corresponding author:

Jacob Ross Bowen

Department of Energy Conversion and Storage, Technical University of Denmark (DTU), Frederiksborgvej 4000, Denmark

Email: jrbo@dtu.dk

Abstract

For solid oxide fuel and electrolysis cells, precise tracking of 3D microstructural change in the electrodes during operation is considered critical to understand the complex relationship between electrode microstructure and performance. Here, for the first time, we report a significant step towards this aim by visualizing a complete redox cycle in a solid oxide cell (SOC) electrode. The experiment demonstrates synchrotron-based ptychography as a method of imaging SOC electrodes, providing an unprecedented combination of 3D image quality and spatial resolution among non-destructive imaging techniques. Spatially registered 3D reconstructions of the same location in the electrode clearly show the evolution of the microstructure from the pristine state to the oxidized state and to the reduced state. A complete mechanical destruction of the zirconia backbone is observed via grain boundary fracture, the nickel and pore networks undergo major reorganization and a the formation of internal voids is observed in the nickel-oxide particles after the oxidation. These observations are discussed in terms of reaction kinetics, electrode mechanical stress and the consequences of redox cycling on electrode performance.

1. **Introduction**

Solid oxide fuel cells (SOFC) and electrolysis cells (SOEC) are promising energy conversion devices due to their operational versatility, high efficiency and potential for exploitation in the renewable energy landscape. SOFCs can produce electrical energy from a large variety of fuels due to their internal hydrocarbon reforming capacity, while SOECs can store electricity from renewable sources as chemical fuels[1–3]. Fluctuating energy demands can be met through reversible operation[4] by switching between these production and storage modes. However, for solid oxide cells (SOCs) to become a robust and competitive energy technology, long-term durability of electrodes and electrolytes under harsh operating conditions is crucial.

State-of-the-art anodes used in SOFCs are based on porous composites of Ni with yttria-stabilised zirconia (YSZ). However, nickel experiences severe dimensional instabilities if the anode is oxidised and SOCs may undergo several redox-cycles during their lifetime. Anode oxidation can occur due to failure in the gas supply system, leakage of oxygen through the electrolyte or under conditions of high fuel utilization[5]. Microstructural changes related to nickel oxidation can lead to fading cell performance or even complete cell failure[5]. Therefore, it is important to understand the nickel oxidation-reduction mechanism in order to predict the potential damage in a cell, leading to a more rational design of oxidation-robust SOC anode electrodes.

Nickel oxidation has previously been investigated using a large number of methods. Transmission electron microscopy (TEM)[6] has been used to study the oxidation of isolated small particles while thermogravimetric analysis (TGA)[7], scanning electron microscopy (SEM)[7], and impedance spectroscopy (IS) [8] have been used to study the effect of the oxidation globally on the entire cermet. However, since the oxidation causes severe modification to the microstructure[7], there is an inherent need to resolve redox phenomena in real cermet electrodes on the microstructure scale in 3D.

Focused ion beam (FIB)-SEM nano-tomography has been used successfully for many 3D electrode degradation studies[9,10] . The technique is characterized by high resolution, good phase contrast and a modest need for sample preparation. It is however an intrinsically destructive technique and thus does not allow “in-situ” or “ex-situ” measurements. To this end X-ray tomography can reconstruct the microstructure of a solid oxide cell non-destructively [11,12]. X-ray Absorption Near Edge tomography [13,14] and X-ray holo-tomography[15,16] are two synchrotron-based techniques that are able to fully reconstruct the SOC 3D microstructure with <50 nm resolution[17]. Holo-tomography has the advantage of using high energy X-rays allowing the analysis of relatively large samples. X-ray

ptychography is a scanning-based realization of a family of coherent diffractive imaging (CDI) techniques where images are produced by combining a set of several far-field scattering patterns obtained with the same coherent, micrometer-sized X-ray probe at overlapping spots[18]. Over the years, ptychography has demonstrated excellent sensitivity to mass density changes and the highest resolution among the X-ray imaging techniques[19].

The non-destructive and quantitative[20] nature of X-ray tomography and the possibility to apply realistic sample environments, allow dynamic *ex-situ* or *in-situ* studies. The first steps in this direction are reported in[21] here nickel particle oxidation was studied using X-ray tomography. However, only 2D projections were acquired and the nickel particles were isolated and not part of a composite electrode. *Shearing et al*.[22] realized the first *ex-situ* oxidation tomography experiment in which a real SOFC electrode microstructure was successfully analyzed after several oxidation steps at different temperatures. However, in their study, only the effect of oxidation was examined and no reduction studies were performed.

The ultimate aim of imaging SOC electrodes in 3D is to visualize and track electrode microstructure evolution during operation to determine the driving forces and their effect on local electrochemical phenomena. A step towards this ambitious aim, the motivation for this work, is performing time-lapse “ex-situ” 3D observations of SOC electrodes after exposure to relevant conditions. In this work,, to our knowledge, we report the first application of ptychographic X-ray computed tomography (PXCT) on SOC electrodes and the first “ex-situ” redox cycling experiment in which the same microstructure is first analyzed in its pristine state and then successively oxidized and reduced.

2. **Experimental methods**

2.1 ***Sample preparation***

The sample was prepared from a typical Ni-3YSZ (Yittria-Stabilized-Zirconia, mol. 3%Y_2O_3) anode supported SOFC half-cell with a ~15 µm thick Ni-8YSZ hydrogen electrode and ~10

µm thick 8YSZ (Yittria-Stabilized-Zirconia, mol. 8%Y_2O_3, mol 8% Y_2O_3) electrolyte. Further details on the cell production can be found elsewhere[23] The NiO-YSZ cermet was reduced for 1h at 850°C. A 3 mm long and 300 µm wide slice was carefully cut using a diamond saw from the reduced half-cell (~300 µm in thickness). The two narrow orthogonal sides of the slice were precision polished (MultiPrep) at an angle to form a truncated asymmetric pyramidal shaped sample with a 60x60 µm square cross section at the top (Figure S1 (b)). This shape has the advantage of being large enough to handle with precision tweezers by hand for sample mounting operations. A standard sample holder compatible with the cSAXS setup [19], was modified in order to accommodate the sample in its center of rotation and minimize sample tilting (see Figure S1 (a)). The sample was mounted on the holder using super glue (Loctite 460, *Loctite Corp.,* ONT) to accurately position the sample. Once cured, the sample was securely attached with platinum paste (CN38-019B Platinum Conductive Paste, *Ferro*) to resist oxidizing and reducing atmospheres at temperatures up to 1000 °C. FIB milling was used to produce a cylindrical pillar: 17 µm in diameter and ~15 µm in height (Figure S1 (c)). FIB milling enables positioning of the imaging volume close to the holder's center of rotation and, more importantly, has the ability to place the electrolyte-electrode interface in the imaged volume.

2.2 ***Tomography procedure***

The nano-tomography experiment was performed at the X12SA (cSAXS) beamline at the Swiss Light Source, Paul Scherrer Institut, Switzerland. The ptychography procedure was carried out at 7.2 keV. The scanning field of view acquired was around 24 by 15 µm with a scanning step of 1.0 µm. At each scanning point, a diffraction pattern was recorded 7.4 m downstream of the object using a Pilatus 2M detector with 172×172 μm^2 pixel size and 0.1 s exposure time. Diffraction patterns with sizes of 400×400 pixels were used in the ptychographic reconstruction, giving an object pixel size of 18.4 nm. For each projection, one thousand iterations of difference map[24] followed by 200 iterations of maximum likelihood

refinement[25] were applied in the reconstruction. For each dataset, 500 projections over an angular range of 180° were collected. Three-dimensional ptychographic computed tomograms[26] were obtained through fine alignment of the reconstructed 2D projections and filtered back projection.

The sample was initially imaged in the pristine state and then subsequently in the fully oxidized and reduced states to form a spatially coherent image of the electrode evolution. The oxidation and the subsequent reduction were performed in a small tube furnace at 850°C with a flow rate of 5 l/h of either air or a gas mixture of 4% H_2 in N_2 respectively. The heating time at maximum temperature was 3h for the oxidation and 1h for the reduction. The ramping rate was 10°C /min for both heating and cooling (**Figure S2** in supplementary materials).

2.3 ***Image analysis, segmentation, registration and microstructural quantification***

Due to the excellent quality and the quantitative nature of the ptychography image data, the raw volumes were easily segmented using a 2D (intensity vs. intensity gradient magnitude) histogram thresholding procedure. Microstructural parameters such as surface areas and percolating triple phase boundary length were calculated as described elsewhere[27].

The oxidized and reduced datasets were registered to the pristine dataset in 3D through a rigid transformation computed by the iterative closest point algorithm[28]. Only points sampled from the YSZ phase were used, allowing registration of the two datasets even under severe changes to the morphology and appearance of the Ni, NiO and pore phases. All the algorithms for segmentation and data analysis were written in-house using MATLAB®.

3. **Results**

3.1. ***Image quality***

The pristine Ni-YSZ anode microstructure studied in this work is presented in **Figure 1**. Figure 1 (a) shows an example of a cross-sectional image slice taken from the raw 3D data-set.

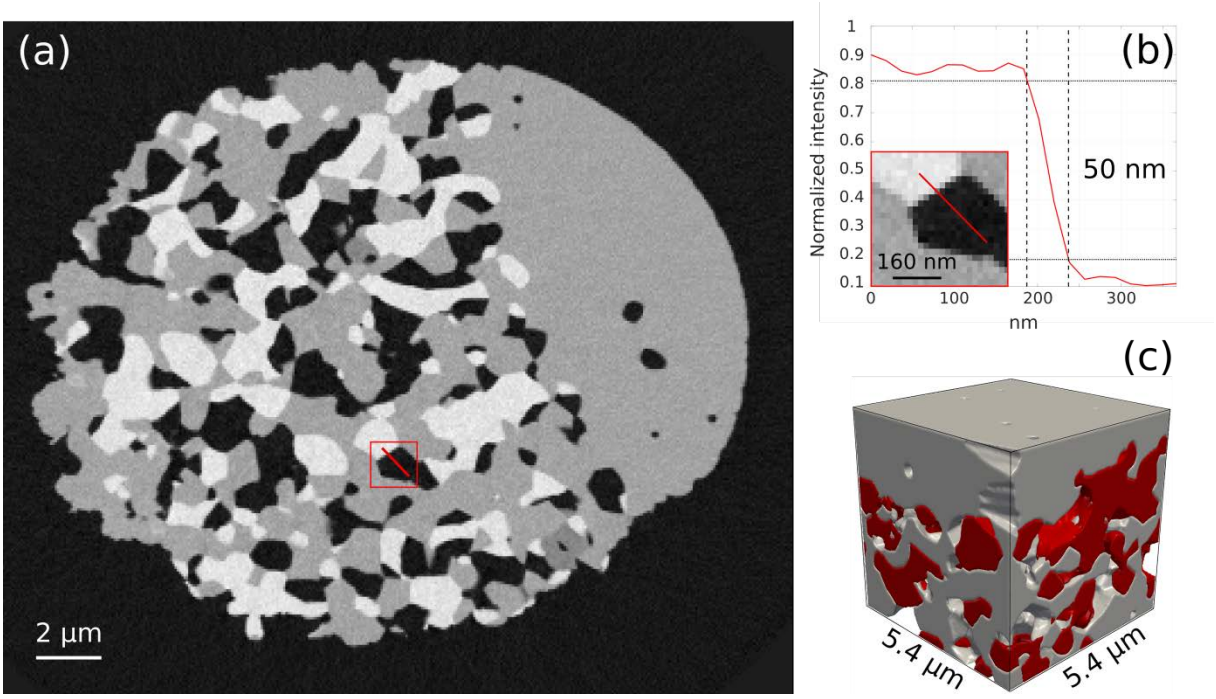

Figure 1. (a) Two-dimensional slice from the entire 3D volume of the pristine Ni-YSZ electrode (raw data). (b) Line profile indicated by the red line in (a) and (b) showing 50 nm resolution by the 10%–90% criteria. (c) Three dimensional rendering of a region containing the electrode-electrolyte interface.

In the image, the bright phase is nickel, the gray phase YSZ and the pores and free space around the sample are dark.

The image contains the electrode-electrolyte interface where the dense electrolyte is seen in the upper right part of the slice. Figure 1(b) shows an intensity profile plot corresponding to the red line indicated in 1(a). Using the 10-90% criteria[19], the 2D resolution is 50 nm while a 3D resolution of 55 nm was calculated from the entire volume using the Fourier shell correlation method[19]. The image in Figure 1(a) shows no significant artifacts and a high signal-to-noise ratio, enabling reliable segmentation. Figure 1(c) shows a 3D sub-volume rendering of the microstructure at the electrode-electrolyte interface.

3.2. ***Overall redox induced microstructural changes***

The effect of the redox-cycle is summarized in **Figure 2** in which slices of the spatially registered volumes are presented.

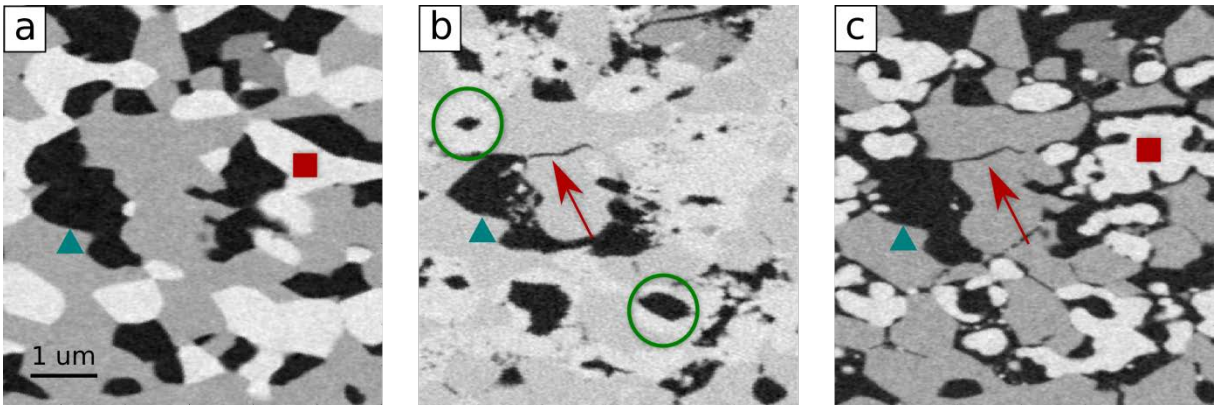

Figure 2. A slice through a sub-volume at identical locations in the electrode in the pristine (a), oxidized (b) and reduced (c) states. In (a) and (c) the pores are depicted in black, the YSZ in gray and the Ni in white. In (b) the brightest phase is NiO. The red arrows in (b) and (c) show the formation of cracks while the green circles in (b) highlight hollow NiO structures. The red rectangle in (a) and (c) indicate locations with a change in the morphology of the nickel phase after the redox cycle. The blue triangles in (a), (b) and (c) mark the same feature in the three different states illustrating the spatial alignment of the volumes.

Triangle markers are used to guide the eye to follow the same individual particles during the redox cycle. The original microstructure (Figure 2a) is directly compared with the oxidized state (Figure 2b) and the reduced state (Figure 3c). In Figure 2b the brightest phase is now NiO and in Figure 2c the intensity of the phases is the same as in (a). Ptychography recovers the material's electron density. The weak contrast in (b) between the solid phases is thus due to the similar electron density of NiO and YSZ. Examining the entire volume confirms that nickel was fully oxidized to nickel-oxide in the sample.

The difference in unit cell volume between nickel (43.9 $Å^3$) and nickel oxide (72.93 $Å^3$)[29]

leads to a considerable volume expansion, resulting in a reduction of total porosity of the sample as seen in Figure 2b. The volume expansion also causes macroscopic deformation during oxidation and the induced stresses fracture the electrode YSZ backbone predominantly at the YSZ grain boundaries as illustrated by the red arrow in Figure 2b.

The resulting microstructure after reduction is shown in Figure 2c. The presence of only three levels of intensity indicates that the NiO has been fully reduced to nickel. Comparing figure Figure 2a and Figure 2c, it is evident that the original microstructure is not recovered and the morphology of nickel and pores change drastically.

For a microstructure statistical analysis, a sub-set of 12x12x12 μm^3 was extracted from the entire dataset. The quantitative analyses are summarized in **Table 1.** From the calculated nickel and YSZ fractions we can calculate that the Ni-YSZ volumetric ratio agrees with the fabrication parameters within 3%. **Figure 3** shows the continuous particles size distribution (PSD) of the same volume in the pristine and reduced state. The present work compares microstructure parameters of the *same* location in the sample as it changes during the redox cycle. Therefore, the analysis is less prone to the issue of representative volume size in contrast to previous studies in which parameters from *different* samples are compared.

Table 1. Microstructural parameters for the analyzed volume in the pristine and reduced state

	Pristine	Reduced	Relative difference [%]
Pore/YSZ interface [$\mu m^2/ \mu m^3$]	1.1	1.5	36.3
Pore/Ni interface [$\mu m^2/ \mu m^3$]	0.5	1.7	240.0
Ni/YSZ interface [$\mu m^2/ \mu m^3$]	1.0	0.6	-41.7
Pore interface [$\mu m^2/ \mu m^3$]	1.7	3.3	94.1
YSZ interface [$\mu m^2/ \mu m^3$]	2.1	2.2	4.7

Ni interface [µm²/ µm³]	1.6	2.4	50.0
Total TPB density [µm/ µm³]	2.7	5.5	105.8
Percolating TPB density [µm/ µm³]	1.9	4.4*	125.0
Nickel phase fraction [-]	0.28	0.29	3.6
YSZ phase fraction [-]	0.47	0.45	-4.2
Pore phase fraction [-]	0.23	0.25	-8.7
Connected Nickel fraction [-]	0.98	0.94	-4
Connected YSZ fraction [-]	0.99	0.99*	0
Connected Pore fraction [-]	0.90	0.99	9

* Not including the effect of the YSZ cracks on the YSZ network connectivity

Based on **Figure 2** and the quantitative analysis, the following observations can be made: i) nickel particles appear smaller and more numerous. The Ni particles mean radius decrease from ~350 nm in the pristine state to ~200 nm in the reduced state and a shift towards smaller particles is observed. However, the fragmentation does not affect considerably the nickel connectivity which only decreases from 98% to 94% of the total nickel phase (**Table 1**).

ii) Nickel particles have become detached from the YSZ and their shape has changed considerably (see the red square in (a) and (c)). The first observation is confirmed by the decrease of the Ni-YSZ interface area (41 %). Furthermore, together with the shift in PSD, the change in shape towards a more fragmented structure contributes to the increase of 91% in total Ni interface area.

iii) Many fine cracks appear at YSZ grain boundaries (red arrows in Figure 2b and Figure 2c). However, because of their limited size, they could not be robustly detected by the segmentation algorithm. This is effect is thus not taken into account in the values for YSZ connectivity and the YSZ particle size distribution presented in **Figure 3**.

iv) The pore structure follows the same behavior as nickel, presenting a shift in the PSD from a mean radius of ~350 nm in the pristine state to ~100 nm after the redox cycle. Furthermore, the connectivity increases from 90% to 99%, likely due to the nickel fragmentation opening new pore pathways between previously isolated pores.

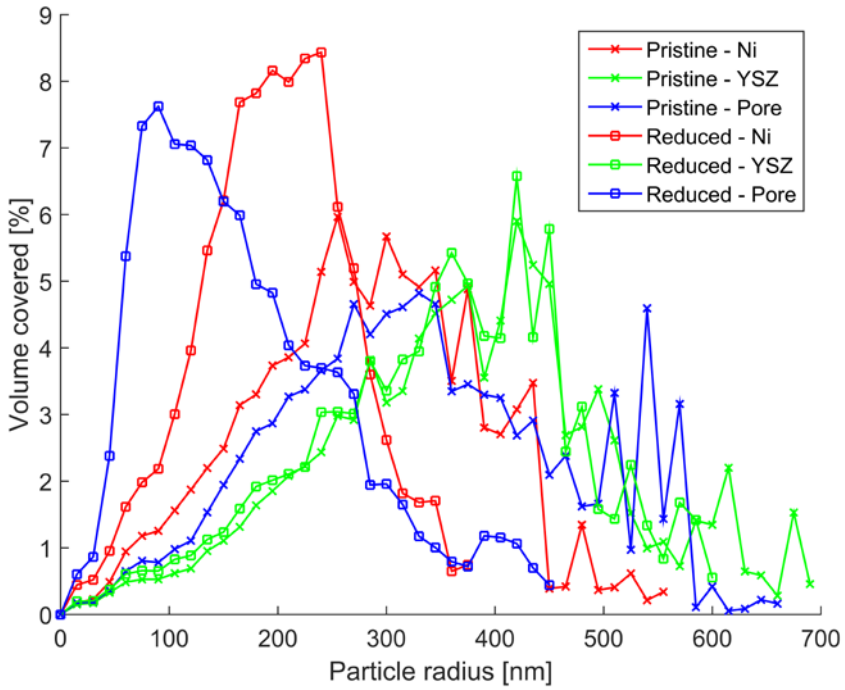

Figure 3. Continuous PSDs of the extracted volumes in the pristine and reduced state including all three phases.

3.3. ***Local effect of the redox cycle***

Figure 4 shows the detailed evolution of the microstructure in a sub-volume representative of many observed locations.

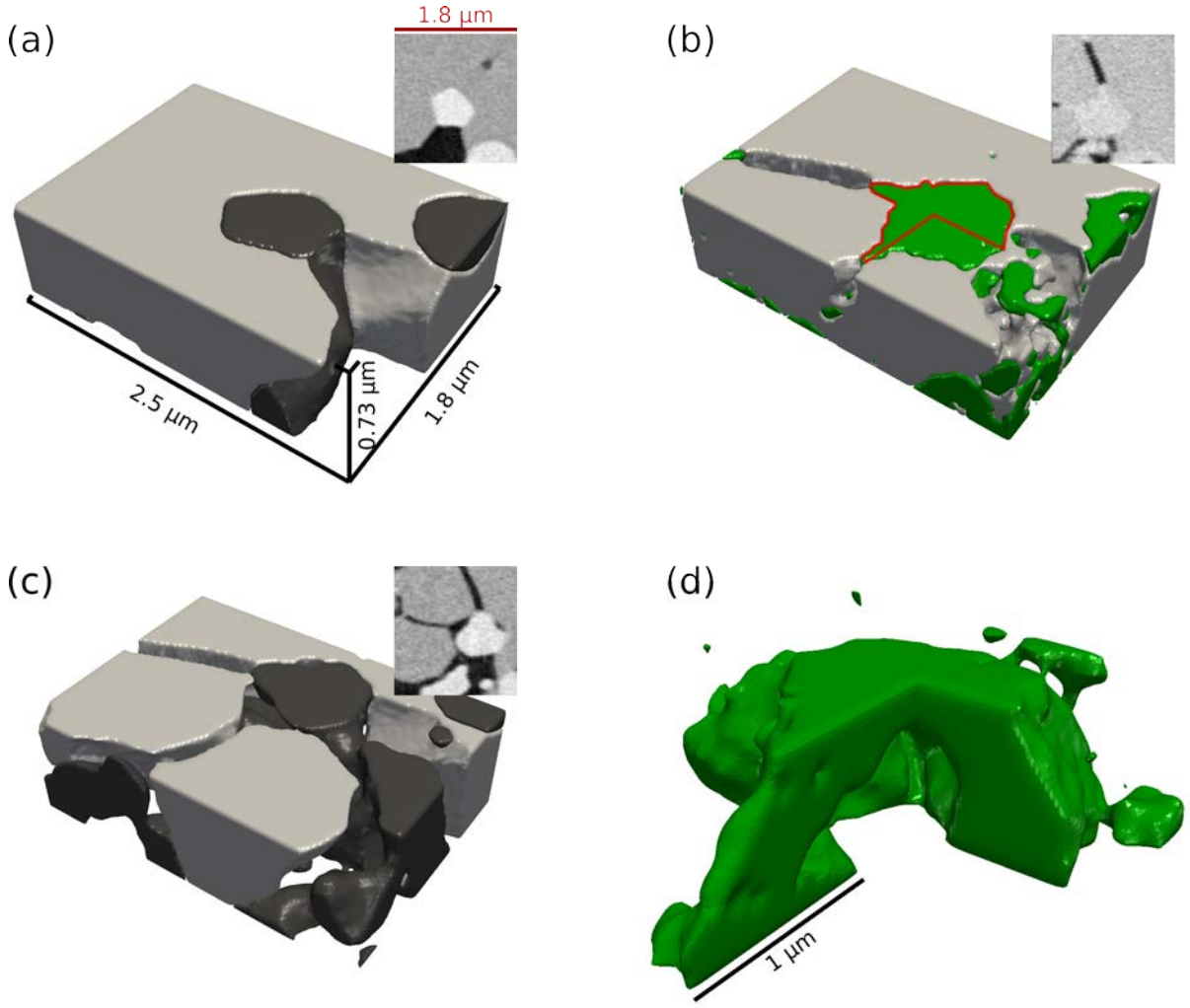

Figure 4. 3D microstructure evolution of a ~ 2.5x1.8 µm size region of the electrode. (a) Pristine, (b) oxidized and (c) reduced state. In the insets, the top two-dimensional slice from the same volume is shown in pristine (a), oxidized (b) and reduced (c) state. (d) a magnified view of the NiO particle presented highlighted by the red contour in (b)

In the pristine state Figure 4a, a nickel particle (black) is surrounded by the YSZ structure (gray). In the oxidized state (Figure 4b) the oxidized nickel particle (green) has expanded in volume and cracks can be observed in the YSZ. We observe that, these cracks correspond to the location of grain boundaries (locations of high YSZ surface curvature) testifying the

presence of intergranular fractures. Moreover, it is observed that the NiO particle protrudes into these cracks. As shown in Figure 2c (green circles) and in Figure 4d, several nickel oxide particles are hollow. These voids can be observed to be completely surrounded by NiO by careful inspection of the surrounding volume, as shown in Figure 4d. The NiO/Pore interfaces appear rough and fragmented.

In the pristine state the nickel particle has a well-defined polyhedral shape (See Figure S4 in Supplementary Materials), dictated by the surrounding YSZ. In Figure 4c the subset volume after the complete redox cycle is presented. The reduced state shows that the nickel has evolved to a more rounded and fragmented structure. Furthermore, the nickel particle is almost completely detached from the YSZ. These structural changes to the Ni phase are observed in the entire sample and their effects can be seen by the decrease in the Ni-YSZ interface area and the increase in Ni-pore surface area (Table 1) from the pristine to the reduced state.

4 **Discussion**

4.1 ***Void formation in NiO particles***

Referring to nickel particle oxidation kinetics for void formation in NiO particles drawing on our observations and reports of Ni oxidation in other systems, we propose the mechanism schematized in **Figure 5**.

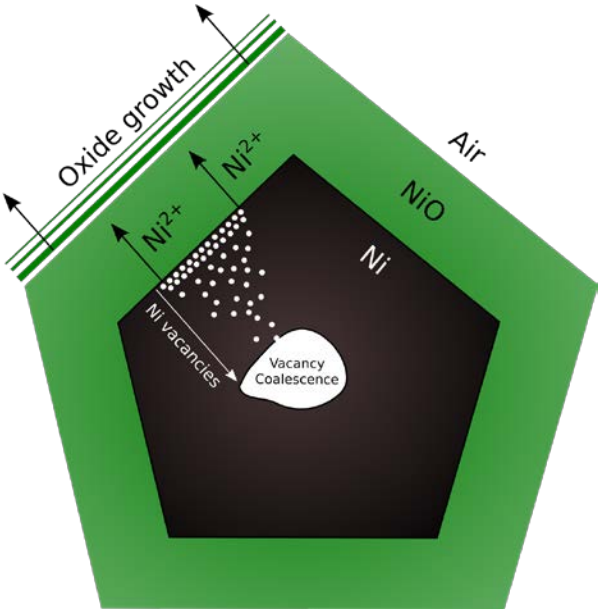

Figure 5. Nickel particles oxidation mechanism. Vacancies and Ni^{2+} ions are injected at the Ni/NiO interface. The Ni^{2+} ions migrate through the NiO layer and react at the NiO/air interface causing the oxide growth. Ni vacancies migrate from the interface to the particle core, resulting in the nucleation and growth of a central void.

Oxidation commences with a thin (several nm) surface oxide layer on Ni particles that nucleates and thickens by ion electro-migration (Cabrera-Mott) while the oxidation mechanism is limited by ion diffusion through the oxide (Wagner)[30]

At the temperature of interest for this work (850 °C), the dominant mass-transport process for NiO growth is the outward migration of Ni ions along NiO grain boundaries and dislocations in the NiO layer[30,31] causing the oxide growth to proceed at the NiO-air interface.

At the oxide-metal interface, Ni cations are supplied to the oxide, either entering lattice interstices or by filling cation vacancies and leave Ni vacancies in the metal at the oxide-metal interface. Such vacancy injection increases the total free energy until is energetically favorable to nucleate voids at the metal-oxide interface or in proximity of defects or impurities. Such phenomena has been described in more detail by Hales and Hill[32] where the oxidation of Ni rods with different surface-volume ratio has been studied.

Void nucleation at the metal-oxide interface in the case of SOC electrodes would lead to failure of the metal-oxide interface generating separated concentric oxide shells[33]. However, such situation is not observed here. Alternatively, in[32] the authors pointed out the possibility that, in presence of impurities, internal voids may nucleate and grow before scale-metal adhesion is lost, permitting continued oxidation and therefore leading to the formation of hollow structures[32]. In this case, void formation by vacancy coalescence could lead to two void morphologies: 1) finely dispersed voids in the NiO network or 2) coalescence to large voids.

The latter situation is in line with the observed morphology of the voids and it is likely the mechanism occurring in this case.

After the initial Ni particle oxidation the proposed mechanism can be briefly summarized: simultaneous outwards migration of Ni^{2+} ions through NiO and injection of vacancies from Ni/NiO interface into Ni; oxide scale grows by outwards migration of NiO/air interface; continual injection of vacancies and the inward migration of the Ni/NiO interface into the shrinking Ni volume creates a driving force for vacancy migration to the Ni particle core, resulting in the nucleation and growth of a central particle void.

4.2 ***YSZ grain boundary cracking and NiO intergranular protrusions***

After oxidation, cracks in the YSZ can be observed throughout the electrode as shown in Figure 2 and Figure 3. During oxidation, the electrode experiences considerable volume expansion generating stress on the YSZ structure. From *2b and 4b*, one can notice that such stress leads to the formation of cracks mainly located at the YSZ grain boundaries. This observation is in line with observations by *Lawrie et al.*[34], who reports the tendency to change from transgranular fracture mode to intergranular mode when fully stabilized YSZ is tested at temperature of 950 ˚C. However, such results were obtained on dense samples

applying the double cantilever mechanical test. Such situations are expected to generate quite different stress distribution within the material.

The fact that we observed mainly intergranular fractures is in line with what was reported by Fouqet et al.[35] and can be explained considering two combined effects:

1. YSZ grain boundaries that intersect Ni-YSZ interfaces are observed to create sharply defined dihedral angles. Therefore, when Ni oxidizes and expands, it acts as a local stress concentrator.
2. NiO protrusions into the YSZ grain boundary cracks act as a wedge producing further stress intensification.

The NiO protrusion formation is considered a direct consequence of the YSZ cracking. Once the crack is formed, new channels for the oxygen are produced and the oxide can grow within the crack itself.

4.3 ***Nickel rearrangement after reduction***

From Figure 3c, it is evident that the original nickel microstructure is not recovered in agreement with previous reports [13]. During cell production, in order to achieve the starting microstructure presented in Figure 2a for the experiment, a sintered cermet NiO-YSZ is reduced at high temperature [1]. Reduction of NiO particles begins with an induction period for the nucleation of metallic clusters which then grow into crystallites[36]. The reduction reaction occurs at the interface between NiO and Ni and it is not controlled by Ni diffusion through the NiO layer (as in the case of oxidation)[37]. Therefore, during the initial NiO reduction, the reaction starts from the exposed surface of the NiO particles and proceeds towards the YSZ structure which acts as a template for the final microstructure. In the case of a cracked YSZ backbone (Figure 2b), hydrogen molecules can permeate the newly created channels.

Thus, the reaction starts radially and proceeds inwards from the NiO particle surface.

Furthermore, once the reduction reaction is complete we speculate that, due to the presence of the observed voids, the Ni particles are free to shrink towards the center of the particle driven by the reduction of Ni-void interface energy producing dense nickel structures. The combined effect of a radial reaction front and the coalescence of the metallic crystallites within the internal voids lead to the nickel contraction away from the YSZ backbone.

Due to the spatial resolution limit, we cannot state if the hollow NiO particles have fractured due to volume expansion induced stresses during oxidation. If this occurs then during reduction fractures would enable hydrogen access to the voids and thus NiO particle reduction may occur from the NiO particle exterior and interior surfaces leading to the Ni particle fragmentation observed in Figure 2c and 3c.

Finally, due to NiO volume contraction on reduction and the corresponding increase in pore volume, Ni surfaces are now free to minimize the surface energy eliminating sharp edges and minimizing the surface curvature. In our experiment the reduction time was designed to ensure complete sample reduction and we do not have access to the time that reduction was completed. Therefore, the Ni microstructure most likely has had significant time for post reduction rearrangement. Studies of the effect of annealing on Ni particle morphology are the topic of future work.

4.4 ***The combined effects of voids, YSZ fracture and Ni particle rearrangement***

The phenomena described in the previous sections have all an impact on the electrode performance. The YSZ cracking is detrimental for the electrode for two reasons: i) the presence of cracks compromises the electrode mechanical properties, and ii) the cracks reduce the ionic conductivity of the YSZ structure by reducing percolation and introducing constrictions in the remaining ionic conduction pathways[27]. The YSZ cracking is a direct effect of the nickel volume expansion of ~70%[5] during oxidation due to the different lattice

parameters and molar volumes between Ni and NiO. However, in many cases as the one presented in Figure 3, the hollow oxide particles occupy a greater volume (volume expansion of ~92% in the case presented in Figure 3) than the one expected based on theoretical calculation. This situation leads to further volume expansion and results in grater overall stress applied to the electrode contributing in the YSZ cracking.

Unlike the YSZ cracking, the nickel detachment is not necessarily detrimental for the electrode. The electrochemical reactions occur only at the triple phase boundaries (TPB)[9] and the Ni-YSZ interface is not electrochemically active. On the other hand, the nickel fragmentation, leads to a considerable increase in the connected TPB density as reported in *table 1*. However, it is unlikely that the presented in Figure 2c and 3c is morphologically stable at high temperature since the Ni particles are expected to coarsen during the operation of the cell to reduce the Ni-pore surface area [1]. Since the nickel fragmentation leads to an increase of TPB density and pore connectivity, we speculate that the YSZ cracking is the main mechanism of electrode degradation during a redox cycle.

The fact that a redox cycle leads to nickel particle fragmentation and increase in TPB density could be used in order to reset the effects of nickel coarsening and return electrodes back towards the optimal nickel particle size distribution. Nickel coarsening is considered a major phenomenon involved in the electrode degradation and leads to nickel particle agglomeration and migration away from the active layer[1]. Thus it is imagined that controlled periodic redox cycles, together with oxidation crack tolerant engineered YSZ microstructures, could be planned during cell lifetime to increase durability.

5. **Conclusions**

Spatially correlated microstructural evolution of a solid oxide cell electrode during a complete redox-cycle was observed using X-ray nano-tomography. For the first time, ptychography is demonstrated as a new tool for the study of SOC electrodes. Ptychographic X-ray nano-

tomography allows detailed 3D microstructural characterization of Ni-YSZ SOC electrodes with high resolution, low noise and unprecedented material phase contrast.

YSZ backbone failure during oxidation occurs predominantly by grain boundary fracture, as many YSZ grain boundaries are located at sites of stress concentration where Ni particles are in contact with YSZ. Furthermore, NiO particles after oxidation present internal voids creating additional volume expansion and therefore mechanical stress during oxidation. Void formation is proposed to be due to vacancy annihilation in metallic nickel during the oxide growth.

After reduction, the electrode does not initially recover its original microstructure. The nickel particles are smaller, with smoother surfaces and are detached from the YSZ structure. The difference in the nickel morphology is a direct consequence of the oxidation. YSZ cracks act as new access channels for hydrogen and thus reduction proceeds radially from the surface towards the center of the particles. Furthermore, contraction towards the internal voids contributes to the nickel detachment from YSZ.

The redox cycle dramatically reduces Ni/YSZ interfacial area, increases the Ni/pore interfacial area and increases the triple phase boundary density. While the YSZ cracking must be avoided to preserve the electrode ionic conductivity and its mechanical integrity, the nickel fragmentation due to the redox cycle could potentially be exploited to reactivate the cell and postpone cell degradation.

Acknowledgements

The authors would like to thank J. Johnson for help in designing and building the sample environment and Xavier Donath for his technical support at the beamline. The authors also thank colleagues at DTU Energy, especially Anne Hauch and Filippo Fennini for valuable input and discussion. Financial support from“the allianCe for ImagiNg of Energy MAterials”, DSF-grant no. 1305-00032B via “The Danish Council for Strategic Research” is gratefully

acknowledged. Travel support for the synchrotron experiment through the DANSCATT grant from the Danish Council for Independent Research is gratefully acknowledged.

Glossary

SOFC Solid Oxide Fuel Cell

SOEC Solid Oxide Electrolysis Cell

SOC Solid Oxide Cell

Ni Nickel

NiO Nickel Oxide

YSZ Yttria-Stabilized-Zirconia

TEM Transmission Electron Microscopy

TGA ThermoGravimetric Analysis

SEM Scanning Electron Microscopy

IS Impedance Spectroscopy

FIB Focused Ion Beam

CDI Coherent Diffractive Imaging

PXCT Ptychographic X-ray Computed Tomography

References

[1] B. Shri Prakash, S. Senthil Kumar, S.T. Aruna, Properties and development of Ni/YSZ as an anode material in solid oxide fuel cell: A review, Renew. Sustain. Energy Rev. 36 (2014) 149–179. doi:10.1016/j.rser.2014.04.043.

[2] S.P. Jiang, S.H. Chan, A review of anode materials development in solid oxide fuel cells, J. Mater. Sci. 39 (2004) 4405–4439. doi:10.1023/B:JMSC.0000034135.52164.6b.

[3] R.J. Kee, H. Zhu, A.M. Sukeshini, G.S. Jackson, Solid Oxide Fuel Cells: Operating Principles, Current Challenges, and the Role of Syngas, Combust. Sci. Technol. 180 (2008) 1207–1244. doi:10.1080/00102200801963458.

[4] C. Graves, S.D. Ebbesen, S.H. Jensen, S.B. Simonsen, M.B. Mogensen, Eliminating degradation in solid oxide electrochemical cells by reversible operation, Nat. Mater. 14 (2015) 239–244. doi:10.1038/nmat4165.

[5] D. Sarantaridis, A. Atkinson, Redox Cycling of Ni-Based Solid Oxide Fuel Cell Anodes: A Review, Fuel Cells. 7 (2007) 246–258. doi:10.1002/fuce.200600028.

[6] S.B. Simonsen, K. Agersted, K.V. Hansen, T. Jacobsen, J.B. Wagner, T.W. Hansen, L.T. Kuhn, Environmental TEM study of the dynamic nanoscaled morphology of NiO/YSZ during reduction, Appl. Catal. Gen. 489 (2015) 147–154. doi:10.1016/j.apcata.2014.10.045.
[7] D. Waldbillig, A. Wood, D.G. Ivey, Thermal analysis of the cyclic reduction and oxidation behaviour of SOFC anodes, Solid State Ion. 176 (2005) 847–859. doi:10.1016/j.ssi.2004.12.002.
[8] T.S. Li, W.G. Wang, H. Miao, T. Chen, C. Xu, Effect of reduction temperature on the electrochemical properties of a Ni/YSZ anode-supported solid oxide fuel cell, J. Alloys Compd. 495 (2010) 138–143. doi:10.1016/j.jallcom.2010.01.103.
[9] J.R. Wilson, W. Kobsiriphat, R. Mendoza, H.-Y. Chen, J.M. Hiller, D.J. Miller, K. Thornton, P.W. Voorhees, S.B. Adler, S.A. Barnett, Three-dimensional reconstruction of a solid-oxide fuel-cell anode, Nat. Mater. 5 (2006) 541–544. doi:10.1038/nmat1668.
[10] J.R. Wilson, J.S. Cronin, S.A. Barnett, Linking the microstructure, performance and durability of Ni-yttria-stabilized zirconia solid oxide fuel cell anodes using three-dimensional focused ion beam–scanning electron microscopy imaging, Scr. Mater. 65 (2011) 67–72. doi:10.1016/j.scriptamat.2010.09.025.
[11] J.R. Izzo, A.S. Joshi, K.N. Grew, W.K.S. Chiu, A. Tkachuk, S.H. Wang, W. Yun, Nondestructive Reconstruction and Analysis of SOFC Anodes Using X-ray Computed Tomography at Sub-50 nm Resolution, J. Electrochem. Soc. 155 (2008) B504–B508. doi:10.1149/1.2895067.
[12] R. Quey, H. Suhonen, J. Laurencin, P. Cloetens, P. Bleuet, Direct comparison between X-ray nanotomography and scanning electron microscopy for the microstructure characterization of a solid oxide fuel cell anode, Mater. Charact. 78 (2013) 87–95. doi:10.1016/j.matchar.2013.02.001.
[13] D. Kennouche, Y.K. Chen-Wiegart, J.S. Cronin, J. Wang, S.A. Barnett, Three-Dimensional Microstructural Evolution of Ni-Yttria-Stabilized Zirconia Solid Oxide Fuel Cell Anodes At Elevated Temperatures, J. Electrochem. Soc. 160 (2013) F1293–F1304.
[14] Y.K. Chen-Wiegart, J.S. Cronin, D. Kennouche, K.J. Yakal-Kremski, S.A. Barnett, J. Wang, Morphological Evolution of Solid Oxide Fuel Cell in Operational Environment With X-Ray Nano-Tomography, in: Meet. Abstr., The Electrochemical Society, 2013: pp. 765–765. https://ecs.confex.com/ecs/224/webprogram/Abstract/Paper24364/B6-0765.pdf (accessed September 8, 2015).
[15] J. Villanova, J. Laurencin, P. Cloetens, P. Bleuet, G. Delette, H. Suhonen, F. Usseglio-Viretta, 3D phase mapping of solid oxide fuel cell YSZ/Ni cermet at the nanoscale by holographic X-ray nanotomography, J. Power Sources. 243 (2013) 841–849. doi:10.1016/j.jpowsour.2013.06.069.
[16] J. Laurencin, R. Quey, G. Delette, H. Suhonen, P. Cloetens, P. Bleuet, Characterisation of Solid Oxide Fuel Cell Ni–8YSZ substrate by synchrotron X-ray nano-tomography: from 3D reconstruction to microstructure quantification, J. Power Sources. 198 (2012) 182–189. doi:10.1016/j.jpowsour.2011.09.105.
[17] J.S. Cronin, Y.K. Chen-Wiegart, J. Wang, S.A. Barnett, Three-dimensional reconstruction and analysis of an entire solid oxide fuel cell by full-field transmission X-ray microscopy, J. Power Sources. 233 (2013) 174–179. doi:10.1016/j.jpowsour.2013.01.060.
[18] M. Dierolf, A. Menzel, P. Thibault, P. Schneider, C.M. Kewish, R. Wepf, O. Bunk, F. Pfeiffer, Ptychographic X-ray computed tomography at the nanoscale, Nature. 467 (2010) 436–439. doi:10.1038/nature09419.

[19] M. Holler, A. Diaz, M. Guizar-Sicairos, P. Karvinen, E. Färm, E. Härkönen, M. Ritala, A. Menzel, J. Raabe, O. Bunk, X-ray ptychographic computed tomography at 16 nm isotropic 3D resolution, Sci. Rep. 4 (2014). doi:10.1038/srep03857.
[20] A. Diaz, P. Trtik, M. Guizar-Sicairos, A. Menzel, P. Thibault, O. Bunk, Quantitative x-ray phase nanotomography, Phys. Rev. B. 85 (2012) 20104. doi:10.1103/PhysRevB.85.020104.
[21] A.M. Kiss, W.M. Harris, S. Wang, J. Vila-Comamala, A. Deriy, W.K.S. Chiu, In-situ observation of nickel oxidation using synchrotron based full-field transmission X-ray microscopy, Appl. Phys. Lett. 102 (2013) 53902. doi:10.1063/1.4789991.
[22] P.R. Shearing, R.S. Bradley, J. Gelb, F. Tariq, P.J. Withers, N.P. Brandon, Exploring microstructural changes associated with oxidation in Ni–YSZ SOFC electrodes using high resolution X-ray computed tomography, Solid State Ion. 216 (2012) 69–72. doi:10.1016/j.ssi.2011.10.015.
[23] A. Hauch, S.D Ebbesen, S.H.Jensen, M. Mogensen, Solid Oxide Electrolysis Cells: Microstructure and Degradation of the Ni/Yittria-Stabilized Zirconia Electrode, J. Electrochem. Soc. 155 (2008) B1184–B1193. doi:10.1149/1.2967311.
[24] P. Thibault, M. Dierolf, A. Menzel, O. Bunk, C. David, F. Pfeiffer, High-Resolution Scanning X-ray Diffraction Microscopy, Science. 321 (2008) 379–382. doi:10.1126/science.1158573.
[25] P. Thibault, M. Guizar-Sicairos, Maximum-likelihood refinement for coherent diffractive imaging, New J. Phys. 14 (2012) 63004. doi:10.1088/1367-2630/14/6/063004.
[26] M. Guizar-Sicairos, J.J. Boon, K. Mader, A. Diaz, A. Menzel, O. Bunk, Quantitative interior x-ray nanotomography by a hybrid imaging technique, Optica. 2 (2015) 259–266. doi:10.1364/OPTICA.2.000259.
[27] P.S. Jørgensen, S.L. Ebbehøj, A. Hauch, Triple phase boundary specific pathway analysis for quantitative characterization of solid oxide cell electrode microstructure, J. Power Sources. 279 (2015) 686–693. doi:10.1016/j.jpowsour.2015.01.054.
[28] P.J. Besl, N.D. McKay, Method for registration of 3-D shapes, in: 1992: pp. 586–606. doi:10.1117/12.57955.
[29] S. Sasaki, K. Fujino, Y. Takéuchi, X-Ray Determination of Electron-Density Distributions in Oxides, MgO, MnO, CoO, and NiO, and Atomic Scattering Factors of their Constituent Atoms, Proc. Jpn. Acad. Ser. B. 55 (1979) 43–48. doi:10.2183/pjab.55.43.
[30] A. Atkinson, Transport processes during the growth of oxide films at elevated temperature, Rev. Mod. Phys. 57 (1985) 437–470. doi:10.1103/RevModPhys.57.437.
[31] A. Atkinson, Growth of NiO and SiO2 thin films, Philos. Mag. Part B. 55 (1987) 637–650. doi:10.1080/13642818708218370.
[32] R. Hales, A.C. Hill, The role of metal lattice vacancies in the hightemperature oxidation of nickel, Corros. Sci. 12 (1972) 843–853. doi:10.1016/S0010-938X(72)80013-1.
[33] H. J. Engel, F. Wever, Old Oxidation, Acta Met. 5 (1957) 695.
[34] M. Dokiya, Proceedings of the Fourth International Symposium on Solid Oxide Fuel Cells (SOFC-IV), The Electrochemical Society, 1995.
[35] D. Fouquet, A.C. Muller, A. Weber, E. Ivers-Tiffee, Oxidation1, Proc 4th Eur. SOFC Forum. (2002) 579.
[36] J.T. Richardson, R. Scates, M.V. Twigg, X-ray diffraction study of nickel oxide reduction by hydrogen, Appl. Catal. Gen. 246 (2003) 137–150. doi:10.1016/S0926-860X(02)00669-5.
[37] T.A. Utigard, M. Wu, G. Plascencia, T. Marin, Reduction kinetics of Goro nickel oxide using hydrogen, Chem. Eng. Sci. 60 (2005) 2061–2068. doi:10.1016/j.ces.2004.11.024.

Supporting Materials

Figure S1

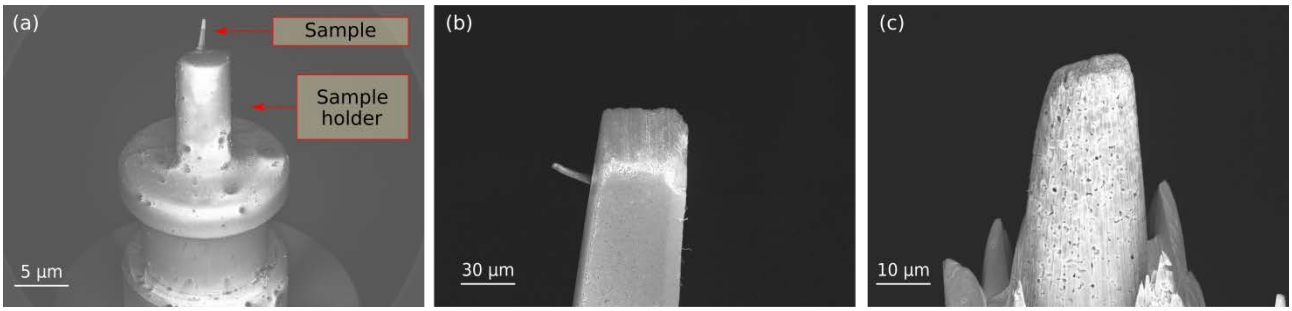

Figure S1. Sample preparation. (a) SEM micrograph of the sample mounted on the sample holder before FIB milling. (b) Highlight of the top of the sample made by precision polishing before FIB milling. (c) Final sample after FIB milling.

Figure S2

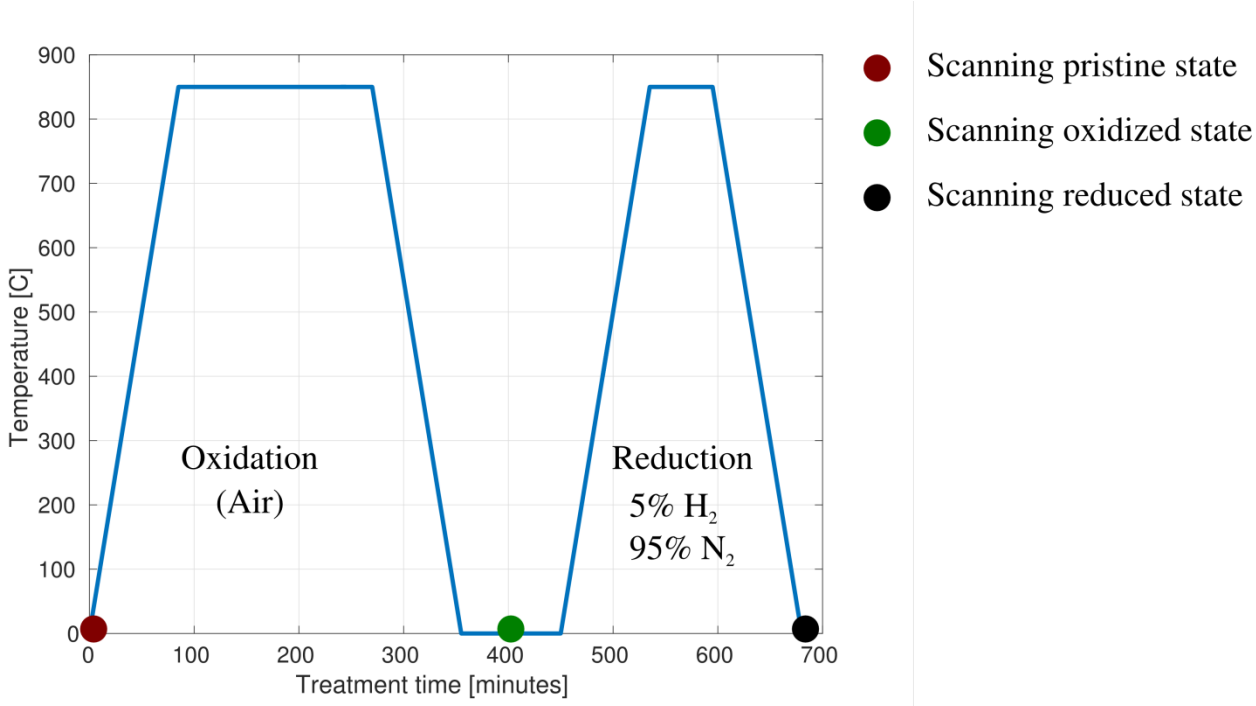

Figure S2. Diagram of the redox-acquisition procedure.

Figure S3

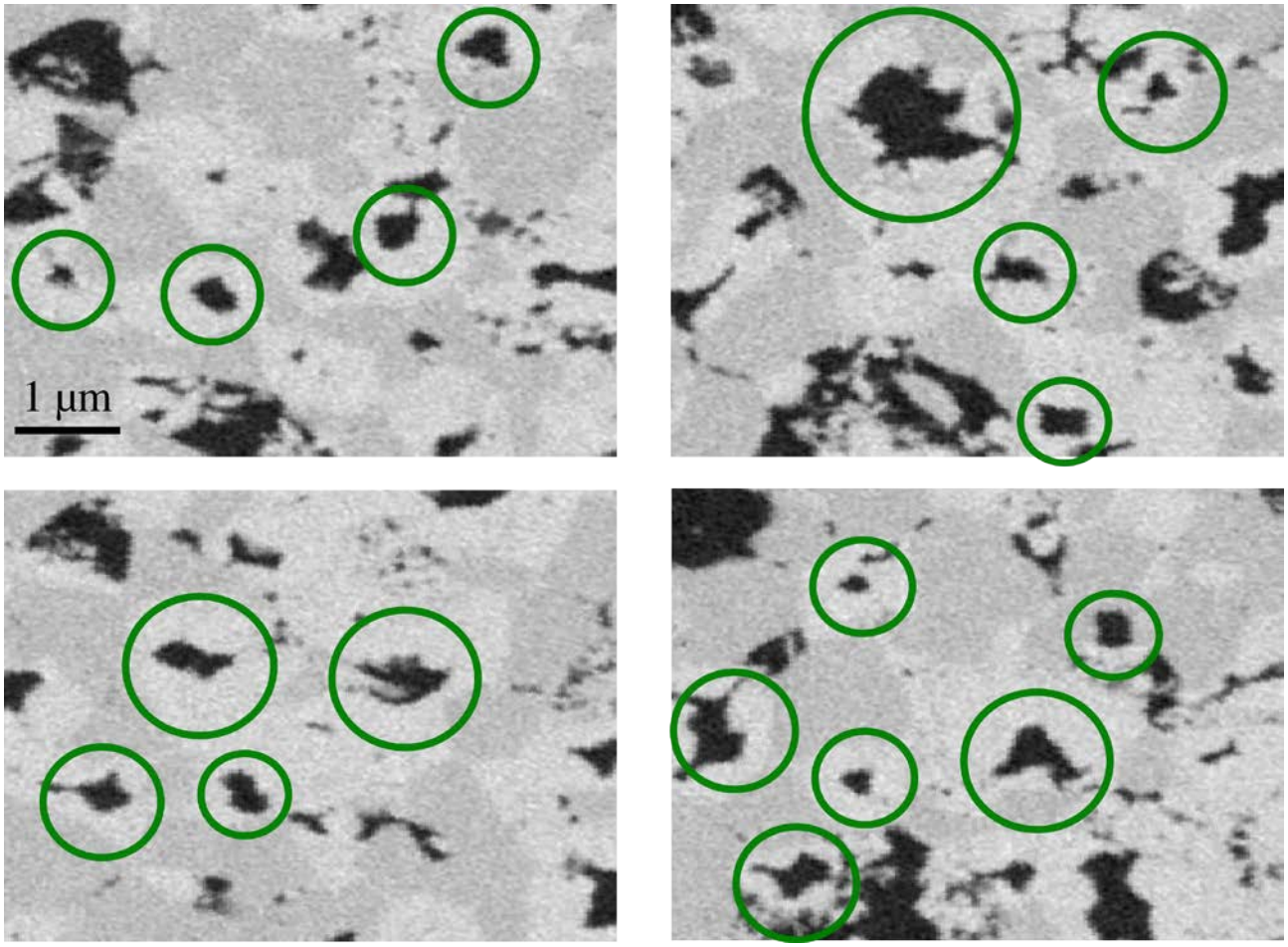

Figure S3: Two-dimensional slices of the entire volume in the oxidized state. The green circles highlight different void formation in the nickel-oxide network. The figure shows that the phenomenon of void formation is present in the entire electrode.

Figure S4

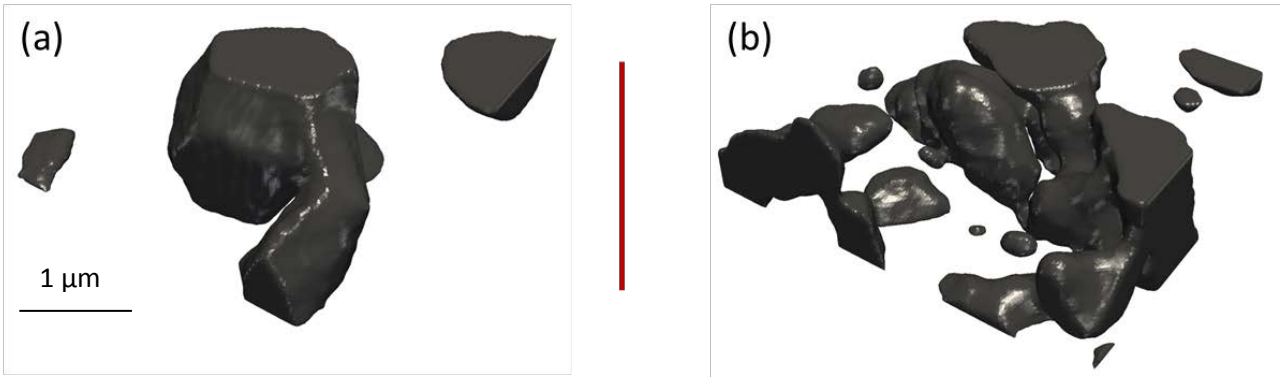

Figure S2. Nickel particle before and after the redox cycle. (a) nickel particle before the redox cycle. (b) nickel particle after the redox cycle.

Figure S5

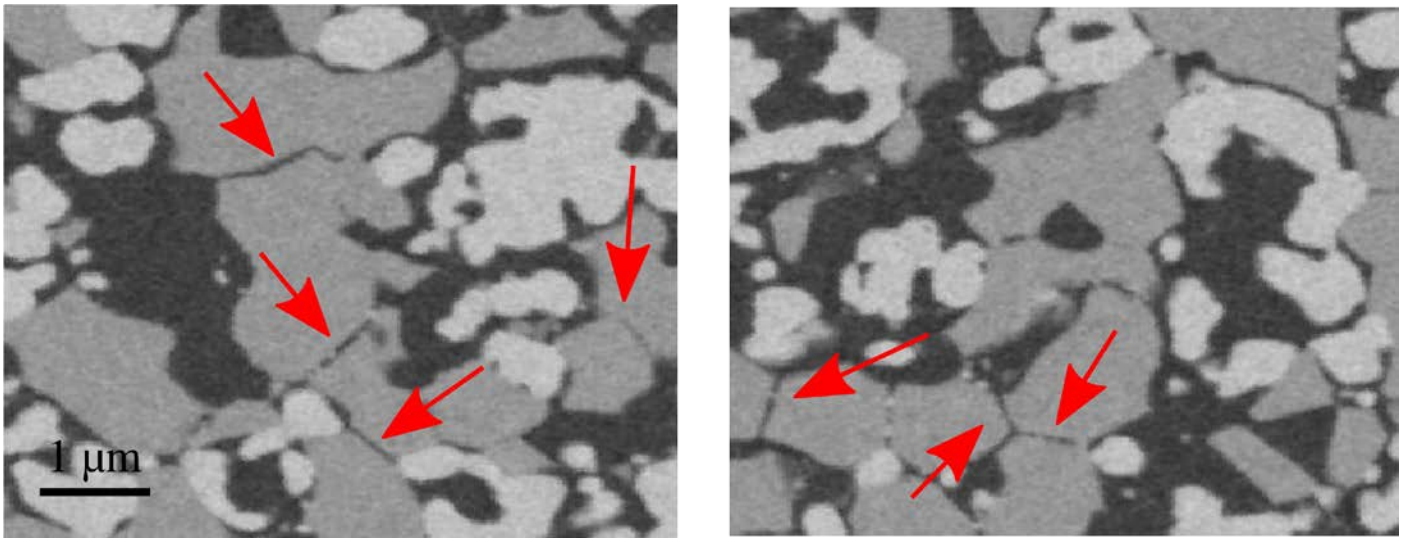

Figure S5. Two-dimensional slices of the entire volume in the reduced state. The red arrows point to several examples of cracks in different parts of the electrode.